



Contents lists available at ScienceDirect

Atmospheric Research

journal homepage: www.elsevier.com/locate/atmosres

Observation of the spectrally invariant properties of clouds in cloudy-to-clear transition zones during the MAGIC field campaign



Weidong Yang^{a,b,*}, Alexander Marshak^a, Patrick J. McBride^c, J. Christine Chiu^d, Yuri Knyazikhin^e, K. Sebastian Schmidt^f, Connor Flynn^g, Ernie R. Lewis^h, Edwin W. Elorantaⁱ

^a Climate and Radiation Branch, NASA, Goddard Space Flight Center, Greenbelt, MD, United States

^b Universities Space Research Association, Columbia, MD, United States

^c Atmospheric & Space Technology Research Associates (ASTRA), Boulder, CO, United States

^d Department of Meteorology, University of Reading, Reading, United Kingdom

^e Department of Geography and Environment, Boston University, Boston, MA, United States

^f Laboratory for Atmospheric and Space Physics, University of Colorado, Boulder, CO, United States

^g Pacific Northwest National Laboratory, PO Box 999, MSIN: K4-28, Richland, WA, United States

^h Environmental and Climate Sciences Department, Brookhaven National Laboratory, Upton, NY, United States

ⁱ Space Science and Engineering Center, University of Wisconsin, Madison, WI, United States

ARTICLE INFO

Article history:

Received 19 January 2016

Received in revised form 2 August 2016

Accepted 7 August 2016

Available online 11 August 2016

Keywords:

Transition zone

Cloud

Cloud-aerosol interaction

Air entrainment and mixing

Spectral invariance

MAGIC field campaign

ABSTRACT

We use the spectrally invariant method to study the variability of cloud optical thickness τ and droplet effective radius r_{eff} in transition zones (between the cloudy and clear sky columns) observed from Solar Spectral Flux Radiometer (SSFR) and Shortwave Array Spectroradiometer-Zenith (SASZe) during the Marine ARM GPCI Investigation of Clouds (MAGIC) field campaign. The measurements from the SSFR and the SASZe are different, however inter-instrument differences of self-normalized measurements (divided by their own spectra at a fixed time) are small. The spectrally invariant method approximates the spectra in the cloud transition zone as a linear combination of definitely clear and cloudy spectra, where the coefficients, slope and intercept, characterize the spectrally invariant properties of the transition zone. Simulation results from the SBDART (Santa Barbara DISORT Atmospheric Radiative Transfer) model demonstrate that (1) the slope of the visible band is positively correlated with the cloud optical thickness τ while the intercept of the near-infrared band has high negative correlation with the cloud drop effective radius r_{eff} even without the exact knowledge of τ ; (2) the above relations hold for all Solar Zenith Angle (SZA) and for cloud-contaminated skies. In observations using redundant measurements from SSFR and SASZe, we find that during cloudy-to-clear transitions, (a) the slopes of the visible band decrease, and (b) the intercepts of the near-infrared band remain almost constant near cloud edges. The findings in simulations and observations suggest that, while the optical thickness decreases during the cloudy-to-clear transition, the cloud drop effective radius does not change when cloud edges are approached. These results support the hypothesis that inhomogeneous mixing dominates near cloud edges in the studied cases.

© 2016 Elsevier B.V. All rights reserved.

1. Introduction

The region between visibly cloudy and cloudless skies, known as the cloud transition zone, is an optically thin mixture of aerosol particles, cloud droplets, and water vapor, with optical thickness decreasing monotonically with distance from the visibly cloudy region. Evidence of the cloud transition zone has been observed from satellites, aircraft, and surface observations. Increasing reflectance with decreasing distance from cloud has been observed in MODIS (Moderate Resolution Imaging Spectroradiometer) data (e.g., Koren et al., 2007; Varnai and

Marshak, 2009). This increase could be the result of small or thin cloud contamination (Zhang et al., 2005; Koren et al., 2009), and/or 3D effects from the nearby cloud (Wen et al., 2006; Marshak et al., 2008). Using 11 years of MODIS data, Chand et al. (2012) observed increased optical thickness that was consistent with hygroscopic growth of aerosol particles in the “cloud halo”, the region near the cloud with increased relative humidity (Perry and Hobbs, 1996; Lu et al., 2003). Similarly increased optical thickness near cloud edge has also been reported from aircraft observations (e.g., Su et al., 2008; Redemann et al., 2009). Its relations with growth of hygroscopic aerosol particles in enhanced relative humidity near cloud (Twohy et al., 2009; Bar-Or et al., 2012) were also investigated. In addition, using instrumentation from the Southern Great Plains (SGP) facility of the Atmospheric Radiation Measurement (ARM) Program, Jeong and Li (2010) found that aerosol

* Corresponding author at: Climate and Radiation Branch, NASA, Goddard Space Flight Center, Greenbelt, MD, United States.

E-mail address: weidong.yang@nasa.gov (W. Yang).

humidification near cloud helped explain about one fourth of the optical thickness–cloud cover correlation.

The size of transition zone can be as large as several kilometers (e.g., Koren et al., 2007; Varnai and Marshak, 2011). However, some studies (Perry and Hobbs, 1996; Lu et al., 2003; Bar-Or et al., 2012) showed that the enhanced humidity near clouds extends to a much smaller scale (hundreds of meters). By excluding the lower confidence aerosol data (that has higher possibility of contamination by undetected optically thin clouds), Yang et al. (2012) found that statistically the size of transition zone could be greatly reduced. It is evident that undetected optically thin clouds play an important role in the radiation properties of the transition zone.

In this paper, we focus on the clouds in the transition zone. These clouds interact and mix with the unsaturated air near cloud edges, thus providing information that can help to improve our understanding of how microphysical properties of clouds can affect cloud-aerosol interactions. For example, the variations of cloud droplet size in the transition zone provide information on identifying the cloud-air mixing mechanisms. Such information is particularly important for improving microphysical parameterizations for cloud simulations (e.g. Korolev et al., 2016).

Basically, the air entrainment and mixing processes can be described by two limiting scenarios: homogeneous and inhomogeneous mixing. Baker et al. (1980) and Baker and Latham (1982) argued that the difference between homogeneous and inhomogeneous mixing could be attributed to the different timescales of mixing and evaporation. Homogeneous mixing results in a drier air penetration into the entire cloud before cloud drops begin to evaporate, leading to a reduction in size of all droplets but no substantial change in the number of cloud droplets. In contrast, with inhomogeneous mixing, evaporation begins before dry air penetrates the entirety of the cloud resulting in a reduction in the droplet number concentration for droplets of all sizes but no change in the cloud drop spectrum (Lehmann et al., 2009; Lu et al., 2013).

Gaining knowledge of the mixing processes has mainly relied on in situ measurements (e.g., Hill and Choulaton, 1985; Gerber et al., 2008; Lehmann et al., 2009, etc.), and, as far as we are aware, has been never observed from ground-based measurements. This paper will demonstrate a novel way to gain such information from ground-based radiation measurements, capitalizing on their high spatial and temporal resolution.

Ground-based observations of the radiative properties of the cloud transition zone have been made with hyperspectral radiometers (e.g., Chiu et al., 2009, 2010; Marshak et al., 2009). In analyzing Atmospheric Radiation Measurement (ARM) Shortwave Spectrometer (SWS) measurements at the ARM SGP site in Oklahoma, a spectrally invariant behavior was found between ratios of zenith radiance spectra during the transition from cloudy to cloud-free air (Marshak et al., 2009). Based on radiative transfer simulations (Chiu et al., 2010), the spectrally invariant behavior of spectral measurements largely depends on cloud optical thickness τ and cloud droplet effective radius r_{eff} . Thus the variation of τ and r_{eff} can be inferred from the analysis of the spectrally invariant behaviors. The droplet size information for optically thin clouds obtained by this approach is based on spectral features of the transition zone, therefore it might be inherently immune to the 3D radiative effects that may affect other methods (e.g. LeBlanc et al., 2015). In this paper, we use an approach similar to Marshak et al. (2009) and Chiu et al. (2010) to understand the cases of cloudy transition zones observed during the Marine ARM GPCI Investigation of Clouds (MAGIC) field campaign (Lewis and Teixeira, 2015). Specifically, we will find the relationship between the spectrally invariant parameters (discussed in more detail in Section 2) and cloud properties such as τ and r_{eff} for low clouds under a mid-latitude summer atmosphere over ocean, a different environmental condition compared to SGP. In addition, we will discuss the spectrally-invariant behavior of the liquid-water absorbing band from 1530 nm to 1660 nm. As such, the simulation results based on these new parameters are suitable to

apply to cloudy transition zones observed by the spectroradiometers during MAGIC.

During the MAGIC field campaign, there were two shortwave spectroradiometer instruments: a Shortwave Array Spectroradiometer-Zenith (SASZe) (<http://www.arm.gov/instruments/sasze>) and a Solar Spectral Flux Radiometer (SSFR) (Pilewskie et al., 2003), both of which measured zenith sky shortwave radiance over the spectral range from the ultraviolet to the near infrared (350 nm–1700 nm) at the sampling frequency of ~1 Hz. However, the SSFR has a spectral resolution between 8 and 12 nm with a field-of-view of 2.8° and the SASZe has a spectral resolution between 1.8 nm and 6 nm with a field-of-view of 1.0°. In this paper, we use redundant measurements from both instruments to help us mitigate instrumental errors or bias, and conclusions about cloud properties will be based on the analysis on independent observations from each instrument.

2. A brief overview of the spectral-invariance method

In observing thin clouds using hyperspectral instruments, Marshak et al. (2009) demonstrated that the transmitted zenith spectra in the transition zone can be well approximated by the linear combination of spectral measurements in cloudy and clear columns. Considering that a cloud moves through the instrument's field of view, a time series of spectra are taken first under cloudy condition (*known_cloudy*), and then under cloudless sky (*known_clear*), with the cloud transition zone (*transition_zone*) in between. (This can be also done starting with the *known_clear* and ending with the *known_cloudy*.) If I is zenith radiance, t is time, then I in the transition zone can be well approximated by a linear combination of zenith radiances in *known-cloudy* and *known-clear* measurements:

$$I(t, \lambda) = a(t) I(t_{\text{known_cloudy}}, \lambda) + b(t) I(t_{\text{known_clear}}, \lambda), \quad (1)$$

where t is between $t_{\text{known_cloudy}}$ and $t_{\text{known_clear}}$ while $a(t)$ and $b(t)$ are the linear coefficients in the linear function. By normalizing both sides of this equation to the spectra of the *known-clear* zenith radiance, it can be rewritten as

$$I(t, \lambda)/I(t_{\text{known_clear}}, \lambda) = a(t) I(t_{\text{known_cloudy}}, \lambda)/I(t_{\text{known_clear}}, \lambda) + b(t), \quad (2)$$

Here $a(t)$ and $b(t)$, which are the slope and intercept in the linear relationship respectively, are dependent on τ and r_{eff} and can be calculated by linear fitting between the normalized spectra $I(t, \lambda)/I(t_{\text{known_clear}}, \lambda)$ and $I(t_{\text{known_cloudy}}, \lambda)/I(t_{\text{known_clear}}, \lambda)$ in Eq. (2). Further studies (Chiu et al., 2010) showed that the normalization by the spectrum of the clear sky substantially mitigates the effects of spectrally dependent aerosol and surface albedo. This leads to an independence (or weakly dependence) of the resulting slopes $a(t)$ and intercepts $b(t)$ on wavelength λ ; thus we call the method as 'spectrally-invariant'. By examining the variations of slope a and intercept b , one can potentially find the corresponding variations of τ and r_{eff} .

3. Methodology and data

The observational cases of cloud transition zones were from the SSFR and SASZe measurements during the MAGIC campaign in July 2013. Due to potential issues in calibrations, the radiance measurements from the two instruments are compared and characterized before being used for the transition zone study.

In observing the cloud in transition zone, we examine the spectral invariance properties of visible (VIS) band (400–870 nm) and near-infrared (NIR) band (1530–1660 nm) at their highest sampling frequency (1 Hz). In addition to the SSFR and SASZe, High Spectral Resolution Lidar (HSRL) (Shipley et al., 1983; Eloranta, 2005) as well as the Total

Sky Imager (TSI) was also used for assisting in the selection of the transition zones where only low water clouds were present.

The dependence of slopes and intercepts on τ and r_{eff} has been understood using simulation results. The radiative transfer calculations were done with the Santa Barbara DISORT Atmospheric Radiative Transfer (SBDART) routine (Ricchiuzzi et al., 1998), using a mid-latitude summer atmosphere and a marine aerosol with an optical thickness of 0.2. Sea water surface type was used in the simulation. A fixed Solar Zenith Angle (SZA) of about 45.6° (corresponding to the cosine of SZA, equal to 0.7) was used for general discussion, except when discussing the sensitivity to μ . Aerosol properties were assumed constant throughout the transition zone, so the calculations will yield information only on the variation in cloud particles. Calculations were done every 3 nm at wavelengths 350–1000 nm, and every 6 nm for wavelengths 1000–1700 nm; these values were chosen to decrease computation time and roughly mimic the spectral sampling of the SSFR and SASZe.

4. Results and discussions

4.1. Dependence of spectral invariance on the cloud optical thickness and droplet effective size

4.1.1. Spectral invariance behaviors from simulations

Fig. 1 shows modeled zenith radiance spectra between 1530 nm and 1660 nm (a) and between 400 nm and 870 nm (b) using the SBDART configuration outlined above. The known cloudy spectrum was modeled with $\tau = 5$ and $r_{\text{eff}} = 8 \mu\text{m}$. The cloud transition zone was modeled with $\tau = 0.5$ and three effective radii: $4 \mu\text{m}$, $8 \mu\text{m}$, and $16 \mu\text{m}$. Finally, the known clear spectrum was modeled with no clouds (i.e., $\tau = 0$). The right panels show the *ratio_to_clear* versus the *cloudy_to_clear* ratio for the respective wavelength range from the left panels and provide verification of the linear relationship. In the upper right panel, the slopes of the three regression lines are almost the

same, but each r_{eff} results in a different intercept. The intercept is related to single scattering albedo ω_0 which (for weakly absorbing wavelengths) is linked to r_{eff} as (Twomey and Bohren, 1980) $1 - \omega_0 \approx ck_{\text{a}} r_{\text{eff}}$, where k_{a} is the bulk absorption coefficient (4π multiplied by the ratio of the imaginary part of the refractive index to wavelength). For liquid water absorbing wavelengths, a larger r_{eff} results in lower ω_0 , which leads to increased absorption and a lower intercept. The intercept and r_{eff} are negatively correlated; thus a decreasing intercept indicates an increasing r_{eff} and vice versa. The right lower panel shows the case of no-absorbing wavelengths; as expected, there is no discernible dependence of either slope or intercept on r_{eff} .

This SBDART simulation shows that under a mid-latitude summer atmosphere over ocean, the approximated linear relationships between the *cloudy-to-clear* and the *ratios-to-clear* described by Eq. (2) are valid for a large range of r_{eff} . In addition, it is evident that the intercepts of NIR band (from 1530 nm to 1660 nm) clearly depend on the r_{eff} and thus the information of the intercepts in this band is well suited to infer cloud droplet size r_{eff} .

4.1.2. Dependency and sensitivity of slopes and intercepts

In order to investigate the details of how the spectral invariant properties vary with τ and r_{eff} , calculations of slopes and intercepts of the spectral invariant method for values of τ between 0.1 and 5 (with step size 0.1) and values of r_{eff} between $4 \mu\text{m}$ and $16 \mu\text{m}$ (with step size $0.1 \mu\text{m}$) are shown in Fig. 2. We have applied the spectrally invariant method separately for the VIS and the NIR spectral regions. The dependence of a_{vis} (slope of VIS band) on τ is clear even for optically thin clouds (Fig. 2a); as the optical thickness decreases, a_{vis} decreases with almost no dependence on r_{eff} . Fig. 2b shows b_{nir} (intercept of NIR band) in the colored contours with the cloud absorption at 1600 nm, calculated as a percentage of the top-of-atmosphere irradiance, overlaid with black contours. These cloud absorption contours help explain the shape of the b_{nir} contours. For the strongest absorption ($>4.5\%$ shown here), b_{nir} and cloud absorption are well correlated and the dependence

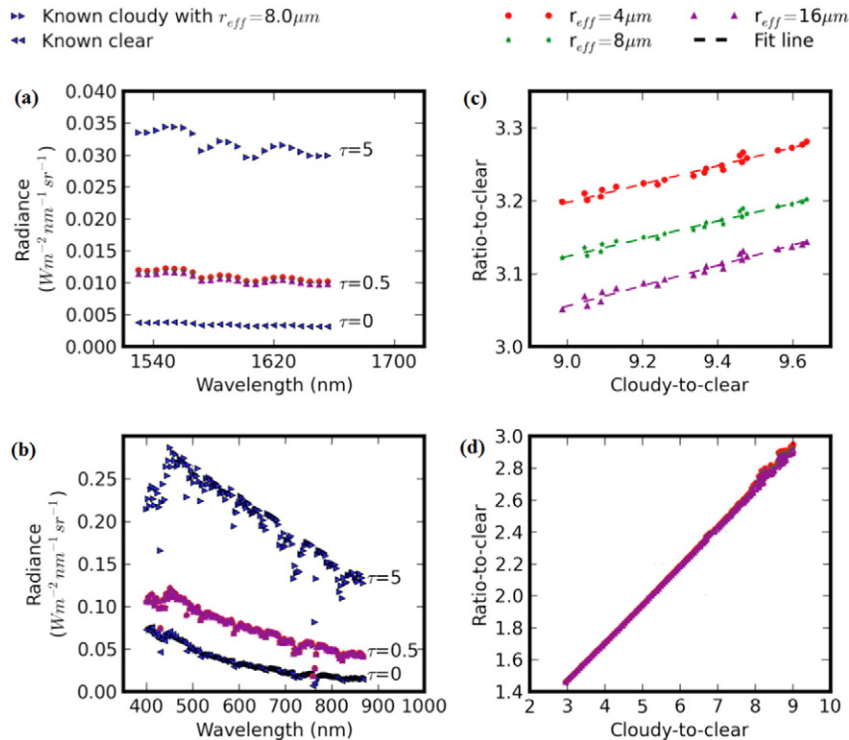


Fig. 1. (a): Modeled spectra between 1530 nm and 1660 nm for three values of cloud optical thickness, $\tau = 5, 0.5$ and 0 . The transition zone optical thickness ($\tau = 0.5$) was calculated for three effective radii, $4, 8$ and $16 \mu\text{m}$. The known cloudy spectrum ($\tau = 5$) was calculated for $r_{\text{eff}} = 8 \mu\text{m}$. (b): Modeled spectra between 400 nm and 870 nm for the same cloud properties. (c)–(d): The corresponding *ratio-to-clear*, $I(\tau = 0.5; r_{\text{eff}} = 4; 8; 16 \mu\text{m})/I(\tau = 0)$, versus the *cloudy-to-clear* ratio, $I(\tau = 5; r_{\text{eff}} = 8 \mu\text{m})/I(\tau = 0)$ for the spectral ranges from the left panels.

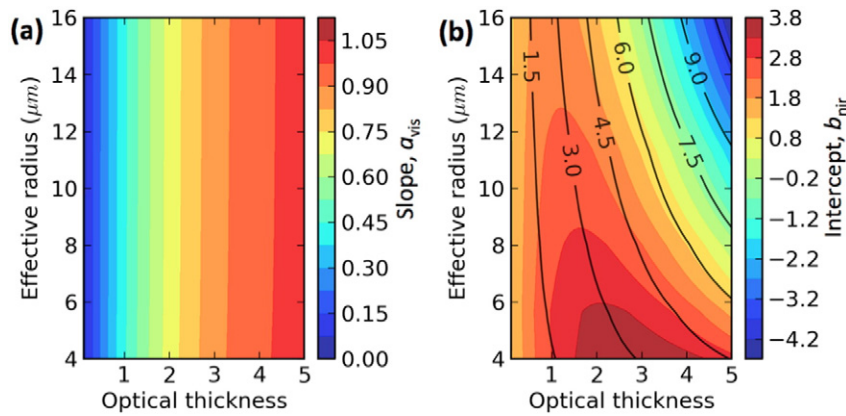


Fig. 2. (a): The slopes of VIS, a_{vis} from Eq. (2) for the spectral range between 400 nm and 870 nm. (b): The intercepts of NIR, b_{nir} from Eq. (2) for the spectral range between 1530 nm and 1660 nm. The black contours show the percentage of cloud absorption at 1600 nm calculated with SBDART. The calculations assume that the known clear value is calculated for $\tau = 0$ and $\mu_0 = 0.7$.

of b_{nir} on r_{eff} is very strong. For absorption between 1.5% and 4.5%, the dependence on r_{eff} and the correlation with absorption lessen, and below the 1.5% absorption contour ($\tau \leq 1$), there is almost no size dependence due to insufficient liquid water absorption. Clearly, in the transition zone analysis, decreasing a_{vis} can be used to indicate decreasing optical thickness as the scene transits from cloudy to cloudless skies while b_{nir} can be used to determine r_{eff} ; increase in b_{nir} indicates decrease in r_{eff} .

To explore the impacts of cloud contamination in the known clear observation, the calculations done for Fig. 2 have been repeated with the known clear spectrum ($\tau = 0$) replaced by a spectrum modeled with $\tau = 0.1$ and $r_{\text{eff}} = 8 \mu\text{m}$. The results (not shown here) indicate that the values of the slope and intercept change, but the shapes of the b_{nir} contours largely stay the same.

To investigate the dependence of zenith radiance and, hence, the slope and intercept of the lines determined by the spectrally invariant technique, on the solar zenith angle, all of the previous calculations were repeated with different values of μ . The test results for other SZA (not shown here) indicate that the solar geometry changes may affect the values of the slope and intercept, but the positive-correlations between τ and a_{vis} and negative-correlations between r_{eff} and b_{nir} remain. Thus, the effect of SZA can be ignored as long as the transition zone does not span a very long time period.

4.1.3. Variability of b_{nir} as a function of r_{eff}

As illustrated in Fig. 2, b_{nir} and r_{eff} are negatively correlated over the included ranges of τ and r_{eff} . However, at lower optical thicknesses ($\tau \leq 1$), there is little or no sensitivity to r_{eff} . In addition, there are also the regions with dual solutions—cases where increase/decrease in b_{nir} corresponds to either increase or decrease in r_{eff} . To quantify the ability of b_{nir} to correctly predict the relative change in r_{eff} , stochastic numerical simulations were run for 10^5 cases, each consisting of two randomly chosen pairs of τ and r_{eff} in the range of Fig. 2. The two points were put in order in such a way that τ was decreasing, to match the assumption in cloudy to clear transitions. Cases where r_{eff} and b_{nir} were negatively correlated were counted as a success. It was found that b_{nir} was able to predict the sign of changes in droplet size in 74% of the 10^5 cases for the conditions as in Fig. 2. For other SZAs, the numbers were in between 73 and 77%.

These high successful rates from numerical experiments above suggest that even without knowing any additional information, b_{nir} can be used as a simple indicator of cloud droplet size in the transition zone: increasing (decreasing) b_{nir} will likely (with probability of $\sim 75\%$) indicate decreasing (increasing) r_{eff} .

4.2. Comparison between SSFR and SASZe zenith radiance measurements in overcast cases

In this section the SSFR and SASZe measurements are compared with those from the Cimel Sunphotometer, a multi-channel, automatic sun-and-sky scanning radiometer that was also deployed in a zenith-pointing “cloud mode” (Chiu et al., 2012) during MAGIC. To match measurements spectrally and temporally, radiance measurements of SSFR and SASZe were averaged over a spectral window of 5 nm and a time window of 5 s centered at the Cimel’s operating wavelength and sampling time. Additionally, considering the differences in field of view and sampling frequency between these instruments, for fairness in comparisons, we use only overcast cases in which zenith radiance signals are stronger and relatively uniform within larger field of views.

In addition to comparing the directly measured spectrum from the instruments, we also further compare the ‘self-normalized’ zenith radiances where we normalized measurements to the initial spectra, i.e., performing $I(t, \lambda)/I(t_0, \lambda)$ with t and t_0 denoting the measurement and initial times. As introduced in Section 2, the spectral invariance method uses normalized radiance spectrum for analyzing cloud properties, instead of the directly measured radiance spectrum.

Fig. 3a–b shows the spectra and time series of measurements for three overcast time periods, with wavelengths (440, 500, 670, 870, and 1640 nm) that match those of Cimel. Additionally, Fig. 3c–d shows the relative deviations of SSFR and SASZe from Cimel before and after ‘self-normalization’, where relative deviation is defined as the difference between unity and the slope of the least-squares fit line between two instrument measurements, for these cases. As an example, if the least-squares fitting line between SSFR (or SASZe) and Cimel has a slope of, say, 1.2, then the relative deviation is 20%, and the relative deviation is zero if the slope of the fitting line is one.

As shown in Fig. 3a–b the measurements from SSFR and SASZe co-vary with those of Cimel. However, the deviations between instruments can be large, sometimes on the order of 30–40%, although the differences have little wavelength dependence (Fig. 3c) and reduce to several percent after self-normalization (Fig. 3d).

The SSFR and SASZe co-vary even on 2015-07-18 when the deviations from Cimel are large, suggesting that the Cimel may have incurred unreliable measurements on this day due to a failure in the wet sensor, allowing sea salt to deposit and interfere with the signal. The consistent deviation between SSFR and SASZe, however, is likely due to different fore-optics, which is being investigated. This intercomparison shows the importance of redundant measurements during such field missions, similarly as implemented in routinely performed measurements at

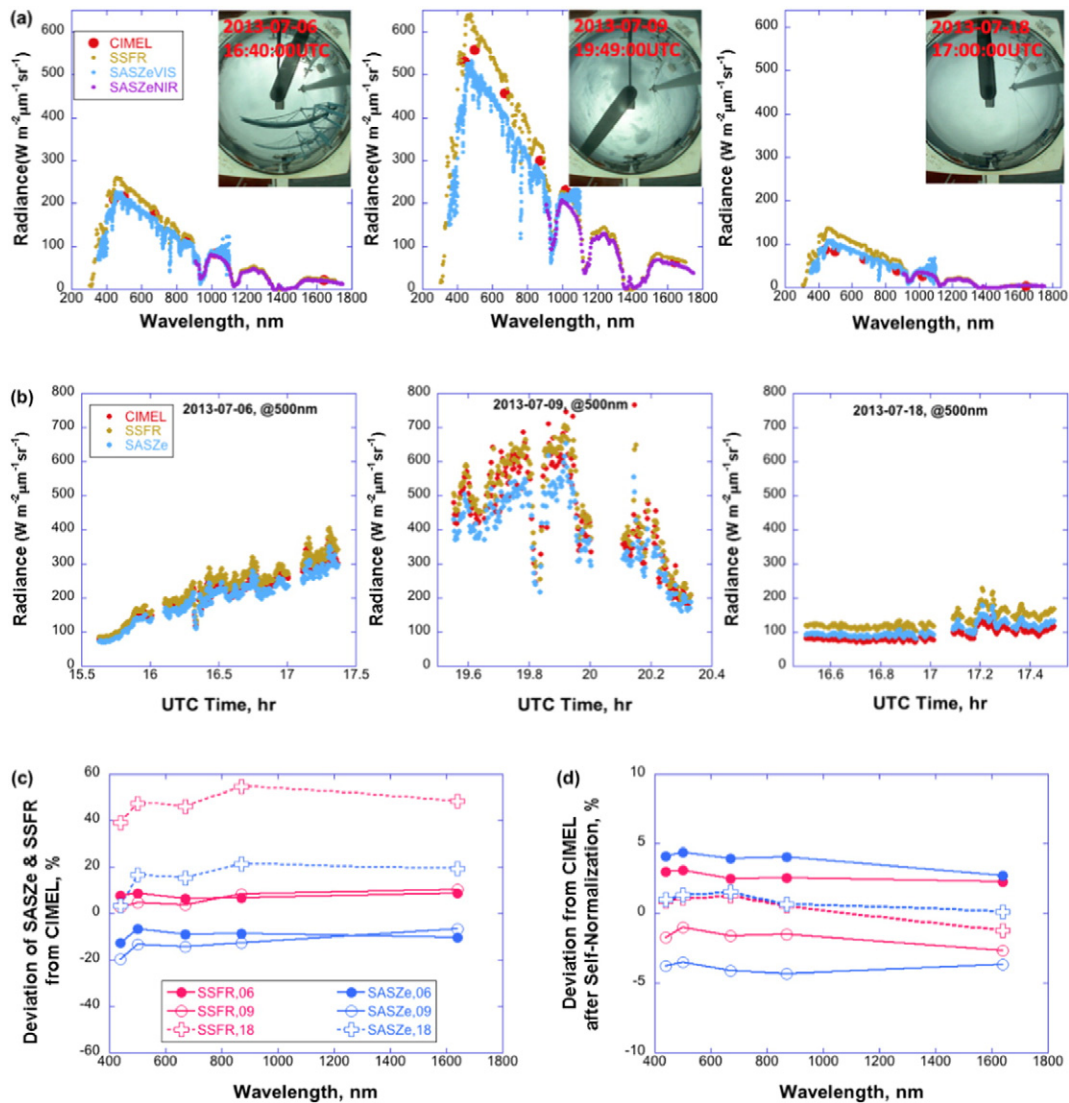


Fig. 3. Comparisons between SASZe, SSFR and CIMEL measurements. (a) Spectra for three overcast cases acquired on 2013-07-06 (left), 2013-07-09 (middle) and 2013-07-18 (right). The insets are TSI images taken at 16:40:00, 19:49:00 and 17:00:00 UTC correspondingly at the three dates. (b) Examples of the time-series at 500 nm corresponding to the three cases in (a). (c) Wavelength dependence of relative deviations of SASZe and SSFR from Cimel in radiation measurements. (d) Same as (c) but after self-normalization.

radiation ground stations such as BSRN (Baseline Surface Radiation Network).

Finally, it is noted that large improvements in reducing the inter-instrument deviations by self-normalization are likely due to a similar spectral behavior of both spectrometers as demonstrated in Fig. 3c. Such improvements suggest that using the self-normalized zenith radiance provides more reliable retrievals compared to those methods that use the absolute radiance measurements. Because the spectral-invariance method described in Section 2 uses spectra of *ratios-to-clear* for both SSFR and SASZe, its results are robust enough as will be demonstrated in the next Section.

4.3. Observations of the transition zones with SSFR and SASZe spectrometers

Two cases of cloud transition zones are used for this study. These two cases are illustrated in Fig. 4 as the transitions from cloudy to clear skies around 01:13 UTC on 2013-07-10 (left) and 00:57 UTC on 2013-07-12 (right). As seen from the backscatter profiles of HSRL and the TSI images in Fig. 4a, the clouds were at an elevation of about 1.4 km and 0.8 km, respectively, and no drizzling was occurring during these times.

Fig. 4b shows the time-series of zenith radiances at 500 nm measured by SSFR, SASZe and Cimel. For the case of 2013-07-10 (left panel), zenith radiances at 500 nm gradually decrease from around 140 to a 40 $\text{W m}^{-2} \mu\text{m}^{-1} \text{sr}^{-1}$ for all three instruments. Since the clear-sky diffused radiation is from molecular and aerosols scattering, zenith radiances at 500 nm at clear skies are much smaller and less variable than that of cloudy skies (unless clouds are optically very thick). The large decrease in the measured radiance indicates that this dataset covers the transition from cloudy sky to clear sky, which starts around 1.2150 h UTC for SSFR and at 1.2125 h UTC for the SASZe and Cimel (a 9 second difference). Similarly, in the case of 2013-07-12 (right panel), the time series of zenith radiances show a transition from much higher value of ~300 to lower and more stable value of ~50; the clear sky region starts at ~0.9530 h UTC for the SSFR and SASZe and at ~0.9520 h UTC for Cimel (a 4 second difference). The differences in the 3 instruments are most likely caused by different fields of view. For convenience, we use 1.2150 h UTC and 0.9530 h UTC as the starting times of the clear skies in the two cases, respectively.

Next we apply the spectrally invariant technique described in Sections 2 and 3 to estimate the slopes at the VIS band and the intercepts at the NIR band. The estimates from SSFR and SASZe are obtained separately by using the same technique. For the case of July 10, we used

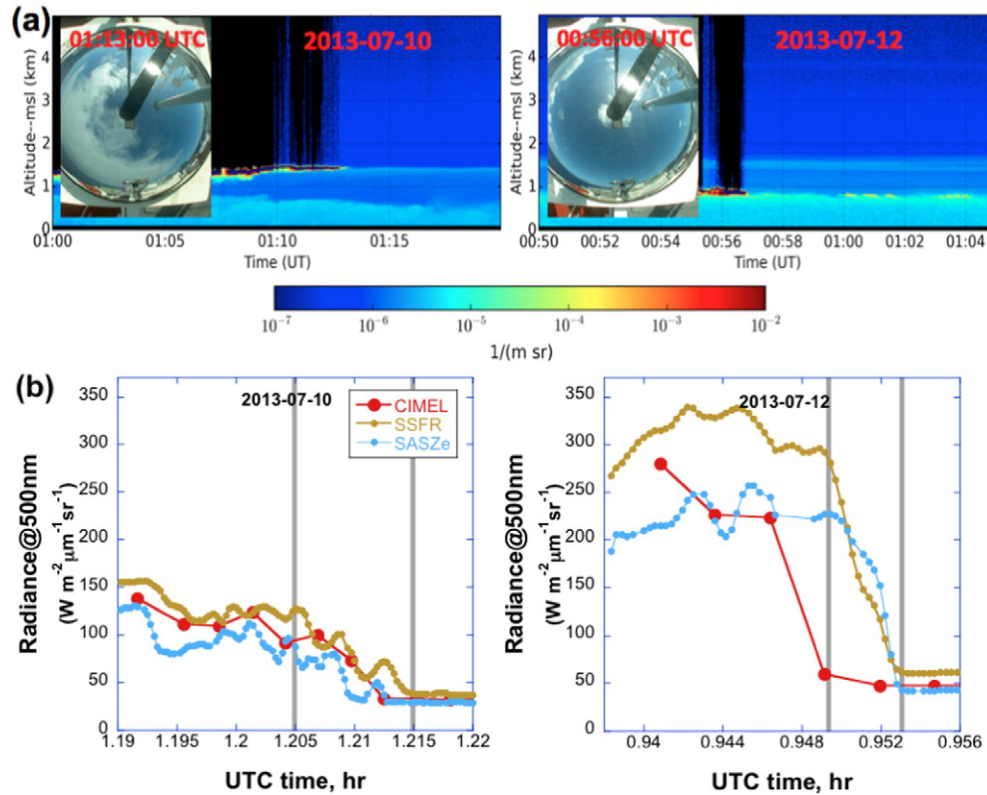


Fig. 4. Two cases of the transition zones. (a) The HSRL lidar backscatter cross-section profiles and the corresponding TSI (Total Sky Imager) images during cloudy-to-clear transitions around UTC time of 01:13 on 2013-07-10 (left) and 00:56 on 2013-07-12 (right). As an example, in the left panel lidar signals are nearly completely attenuated before $\sim 01:13$, indicating cloudy situations; and afterwards is clear. (b) The zenith radiance measurements at 500 nm from Cimel, SSFR and SASZe on 2013-07-10 (left), and on 2013-07-12 (right). The transition regions discussed in this paper are between grey vertical lines for each case. It is estimated that the sizes of the corresponding regions are ~ 280 m and ~ 100 m for left and right cases, respectively (see text for details).

1.1900 h UTC and 1.2200 h UTC as the times for *known-cloudy* and the *known-clear* skies, respectively. While for 2013-07-12, they are 0.9380 h UTC and 0.9560 h UTC, respectively. Additionally, we focus only on the part of the transition zone right around the cloud edge, as illustrated by the area between the two vertical grey lines in each case of Fig. 4b. By using the cloud-base altitude information from HSRL and the angular speed of moving cloud relative to the ship from sequential TSI images, we estimated that cloud relative speeds are ~ 8 m/s in both cases. Therefore, the sizes of transition regions here are ~ 280 m for case of 2013-07-10 and ~ 100 m for case of 2013-07-12, respectively.

The time-series of a_{vis} and b_{nir} from the two instruments on 2013-07-10 are shown in Fig. 5a–b. Both instruments show a decreasing trend in a_{vis} with time (Fig. 5a) that indicates the decrease in optical thickness τ towards the cloud edge. Because of the high anti-correlations between the r_{eff} and b_{nir} , Fig. 5b seems to imply a slight decrease in r_{eff} determined from SSFR measurements and slight increase in r_{eff} determined from SASZe measurements towards the cloud edge. The opposing results from the SSFR and SASZe are due to the measurement differences of the two instruments as discussed in Section 4.2. To mitigate the effects from instruments, here we weigh the data from the two instruments equally and use a linear function to fit the combined intercepts to show the trends. As such, the combined results from two instruments depict a nearly constant intercept; thus no significant size changes near cloud edges have been observed (black line in Fig. 5b which is the best linear fit of the averaged intercepts of SSFR and SASZe).

Similar to Fig. 5a, Fig. 5c shows that both instruments yield a decreasing trend in a_{vis} , indicating the decrease of τ towards cloud edge on 2013-07-12. Unlike Fig. 5b, Fig. 5d shows rather significant increase in b_{nir} from both instruments for ~ 4 s before b_{nir} reaches a nearly constant value near the cloud edge. This feature is clearly illustrated by

the linear fits of the mean intercepts of SSFR and SASZe (black lines in Fig. 5d). This result indicates that in this time period (0.94917 h to 0.95000 h UTC), the r_{eff} likely decreases first and then remains unchanged until the cloud edge is reached. It is noted that due to finite fields of view, the horizontal resolution at altitude of 0.8 km is about ~ 14 m for the SASZe and ~ 39 m for the SSFR. Considering that the estimated horizontal wind speed was ~ 8 m/s, we can see that radiance values that are 2 s (SASZe) and 5 s (SSFR) before the cloud edge are significantly affected by clear-sky columns, and are thus not included.

The variation features of slopes and intercepts near the cloud edges in the above two cases demonstrate interesting cloud properties due to mixing with dry air in transition zones. Since the inhomogeneous mixing hypothesis predicts no change in cloud drop effective radius, the results in Fig. 5b and d indicate that inhomogeneous mixing dominates near the cloud edges on both cases. Meanwhile, since the homogeneous mixing hypothesis leads to prediction of decrease in cloud drop size, results in Fig. 5d indicate a homogeneous mixing is likely dominant in the region next to the inhomogeneous mixing region near the cloud edge.

These spectral-invariance-based results on inhomogeneous mixing near the cloud edge are consistent with the recent findings in direct holographic in-situ microscopic measurements (Beals et al., 2015) and theoretical analysis (e.g. Korolev et al. 2016), whose findings demonstrated that interaction between cloud and dry air is dominated by inhomogeneous mixing, especially near the cloud edge. In addition, the results on homogeneous mixing are also consistent with the findings of earlier works (e.g. Lehmann et al., 2009). Their findings suggested that homogeneous mixing be more likely to occur in the vicinity of the cloud core, whereas inhomogeneous mixing dominates in more diluted cloud regions.

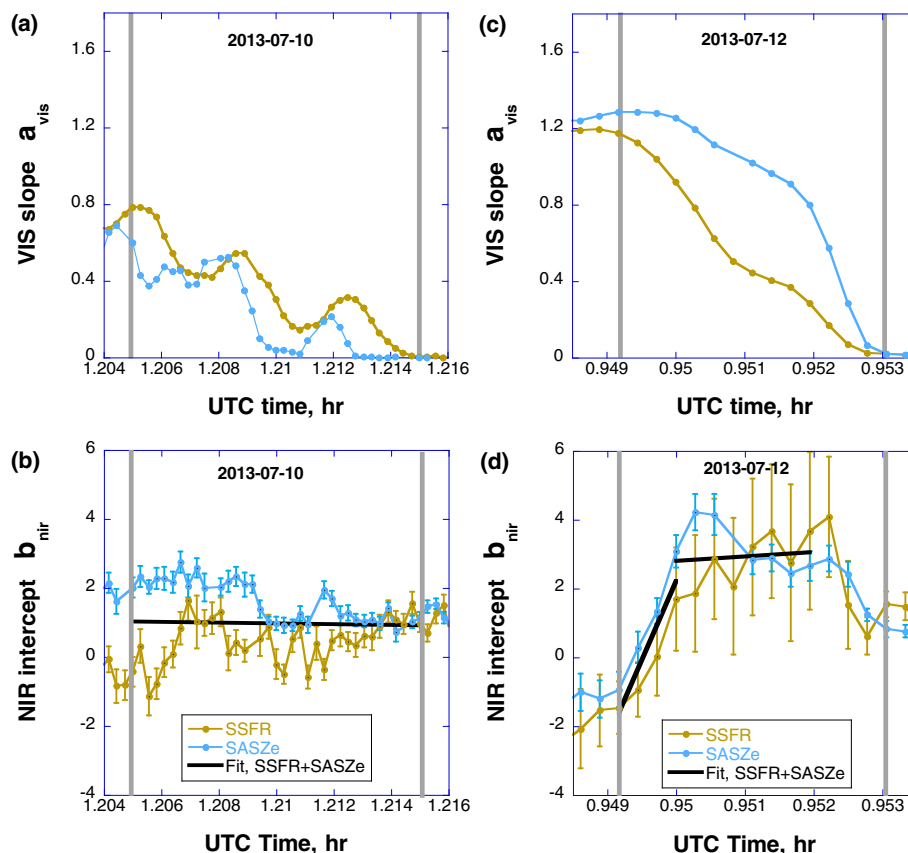


Fig. 5. Time-series of a_{vis} and b_{nir} for both SSFR and SASZe observations. Left column corresponds to 2013-07-10 while right column to 2013-07-12. (a) and (c) are slopes of the visible spectral region; (b) and (d) are intercepts of the NIR spectral region. The black lines in (b) and (d) are fits of the average intercepts for both instruments near cloud edges.

5. Summary

Knowledge of variability of cloud properties in the transition zones between cloudy and clear air is important for understanding the mechanisms of cloud-aerosol interactions. This paper uses the spectral-invariance method developed earlier to understand how the size of cloud droplets varies in the transition zones observed during the MAGIC field campaign.

We first used a simplified SBDART model that contains a single layer low cloud in a mid-latitude summer atmosphere over ocean to test the assumptions of the spectrally-invariant technique in the transition zone. It was shown that for the VIS spectral region the slope of the linear relationships defined by Eq. (2) decreases with decreasing cloud optical thickness τ while for the NIR spectral region (from 1530 nm to 1660 nm) the intercept is highly anti-correlated with cloud drop effective radius r_{eff} . This relationship remains for all SZA and is not sensitive to cloud contaminations if the clear sky region is not accurately determined. The highly anti-correlated relationship between the b_{nir} and r_{eff} sizes was demonstrated using statistical numerical experiments: in ~75% of all cases lower values of b_{nir} corresponded to higher values of r_{eff} .

Cloud transition zones were observed in the measurements of zenith radiances by the two independent spectrometers (SSFR and SARZe) during the MAGIC field campaign. The measurements from these two instruments were quite different, however the difference of the self-normalized measurements between the two instruments was relatively small. Two cases with low, non-drizzling clouds were selected for the transition zone study.

Although the two transition zones were different in many aspects, we found that both demonstrated the same spectrally-invariant properties near cloud edges. In particular, when the cloud edges are

approached, the slopes of the VIS region decreased while intercepts of the NIR spectral region estimated from the two instruments remained nearly constant. These features clearly indicate that cloud droplet effective sizes do not change much near cloud edges. This is consistent with recent in-situ measurements (e.g. Beals et al., 2015). To the best of our knowledge, this work is the first attempt to use ground-based remote sensing instruments for understanding the entrainment and mixing issues near cloud edges.

Acknowledgments

This research was supported by the Office of Science (BER), U.S. Department of Energy (DOE), under grant DE-SC0005457. J. C. Chiu was supported by the Office of Science (BER), U.S. Department of Energy (DOE) under grant DE-SC0011666. E. Lewis was supported by the U.S. Department of Energy's Atmospheric System Research Program (Office of Science, BER) under Contract No. DE-SC00112704. Thanks to Warren Gore of NASA Ames Research Center for his support of the SSFR during MAGIC. We thank Horizon Lines and the Captain and crew of the *Horizon Spirit* for their support and hospitality during MAGIC. We would also like to thank David Troyan and Tami Toto for ship movement correction; and Laurie Gregory, Richard Wagener and Cimel Electronique for their help with deploying the Cimel sun photometer on the ship. The MAGIC data can be found at <http://www.arm.gov/campaigns/amf2012magic>.

References

- Baker, M.B., Latham, J., 1982. A diffusive model of the turbulent mixing of dry and cloudy air. *J. R. Meteorol. Soc.* 108, 871–898. <http://dx.doi.org/10.1002/qj.49710845809>.

- Baker, M.B., Corbin, R.G., Latham, J., 1980. The influence of entrainment on the evolution of cloud droplet spectra: I. A model of inhomogeneous mixing. *Q. J. R. Meteorol. Soc.* 106, 581–598. <http://dx.doi.org/10.1002/qj.49710644914>.
- Bar-Or, R.Z., Koren, I., Altaratz, O., Fredj, E., 2012. Radiative properties of humidified aerosols in cloudy environment. *Atmos. Res.* 118, 280–294. <http://dx.doi.org/10.1016/j.atmosres.2012.07.014> ISSN 01698095.
- Beals, M.J., Fugal, J.P., Shaw, R.A., Lu, J., Spuler, S.M., Stith, J.L., 2015. Holographic measurements of inhomogeneous cloud mixing at the centimeter scale. *Science* 350 (6256), 87–90. <http://dx.doi.org/10.1126/science.aab0751>.
- Chand, D., Wood, R., Ghan, S.J., Wang, M., Ovchinnikov, M., Rasch, P.J., Miller, S., Schichtel, B., Moore, T., 2012. Aerosol optical depth increase in partly cloudy conditions. *J. Geophys. Res.* 117, D17207. <http://dx.doi.org/10.1029/2012JD017894>.
- Chiu, J.C., Marshak, A., Knyazikhin, Y., Pilewskie, P., Wiscombe, W.J., 2009. Physical interpretation of the spectral radiative signature in the transition zone between cloud-free and cloudy regions. *Atmos. Chem. Phys.* 9 (4), 1419–1430. <http://dx.doi.org/10.5194/acp-9-1419-2009>.
- Chiu, J.C., Marshak, A., Knyazikhin, Y., Wiscombe, W.J., 2010. Spectrally-invariant behavior of zenith radiance around cloud edges simulated by radiative transfer. *Atmos. Chem. Phys.* 10 (22), 11295–11303. <http://dx.doi.org/10.5194/acp-10-11295-2010>.
- Chiu, J.C., Marshak, A., Huang, C.H., Varnai, T., Hogan, R.J., Giles, D.M., Holben, B.N., O'Connor, E.J., Knyazikhin, Y., Wiscombe, W.J., 2012. Cloud droplet size and liquid water path retrievals from zenith radiance measurements: examples from the Atmospheric Radiation Measurement Program and the Aerosol Robotic Network. *Atmos. Chem. Phys.* 12 (21), 10313–10329. <http://dx.doi.org/10.5194/acp-12-10313-2012>.
- Eloranta, E., 2005. *High Spectral Resolution Lidar*. In: Weikamp, K. (Ed.), *Lidar: Range Resolved Optical Remote Sensing of the Atmosphere*. Springer, pp. 143–163.
- Gerber, H., Frick, G., Jensen, J.B., Hudson, J.G., 2008. Entrainment, mixing, and microphysics in trade-wind cumulus. *J. Meteorol. Soc. Jpn.* 86, 87–106.
- Hill, T.A., Choulaton, T.W., 1985. An airborne study of the microphysical structure of cumulus clouds. *Q. J. R. Meteorol. Soc.* 111, 517–544.
- Jeong, M., Li, Z., 2010. Separating real and apparent effects of cloud, humidity, and dynamics on aerosol optical thickness near cloud edges. *J. Geophys. Res.* 115 (D7), D00K32. <http://dx.doi.org/10.1029/2009jd013547>.
- Koren, I., Remer, L.A., Kaufman, Y.J., Rudich, Y., Martins, J.V., 2007. On the twilight zone between clouds and aerosols. *Geophys. Res. Lett.* 34 (8), L08805. <http://dx.doi.org/10.1029/2007GL029253>.
- Koren, I., Feingold, G., Jiang, H., Altaratz, O., 2009. Aerosol effects on the inter-cloud of a small cumulus cloud field. *Geophys. Res. Lett.* 36 (14), L14805. <http://dx.doi.org/10.1029/2009gl037424>.
- Korolev, A., Khain, A., Pinsky, M., French, J., 2016. Theoretical study of mixing in liquid clouds – part 1: classical concepts. *Atmos. Chem. Phys.* 16 (9235–9254), 2016. <http://dx.doi.org/10.5194/acp-16-9235-2016>.
- LeBlanc, S.E., Pilewskie, P., Schmidt, K.S., Coddington, O., 2015. A spectral method for discriminating thermodynamic phase and retrieving cloud optical thickness and effective radius using transmitted solar radiance spectra. *Atmos. Meas. Tech.* 8, 1361–1383. <http://dx.doi.org/10.5194/amt-8-1361-2015>.
- Lehmann, K., Siebert, H., Shaw, R.A., 2009. Homogeneous and inhomogeneous mixing in cumulus clouds: dependence on local turbulence structure. *J. Atmos. Sci.* 66, 3641–3659. <http://dx.doi.org/10.1175/2009JAS3012.1>.
- Lewis, E.R., Teixeira, J., 2015. Dispelling clouds of uncertainty. *Eos* 96 (12), 16–19. <http://dx.doi.org/10.1029/2015EO031303> 2015.
- Lu, M., Wang, J., Flagan, R.C., Seinfeld, J.H., Freedman, A., McClatchey, R.A., Jonsson, H.H., 2003. Analysis of humidity halos around trade wind cumulus clouds. *J. Atmos. Sci.* 60 (8), 1041–1059. [http://dx.doi.org/10.1175/1520-0469\(2003\)60<1041:AOHHAT>2.0.CO;2](http://dx.doi.org/10.1175/1520-0469(2003)60<1041:AOHHAT>2.0.CO;2).
- Lu, C., Liu, Y., Niu, S., Krueger, S.K., Wagner, T., 2013. Exploring parameterization for turbulent entrainment-mixing processes in clouds. *J. Geophys. Res. Atmos.* 118, 185–194. <http://dx.doi.org/10.1029/2012JD018464>.
- Marshak, A., Wen, G., Coakley, J.A., Remer, L.A., Loeb, N.G., Cahalan, R.F., 2008. A simple model for the cloud adjacency effect and the apparent bluing of aerosols near clouds. *J. Geophys. Res.* 113 (D14), D14S17. <http://dx.doi.org/10.1029/2007jd009196>.
- Marshak, A., Knyazikhin, Y., Chiu, J.C., Wiscombe, W.J., 2009. Spectral invariant behavior of zenith radiance around cloud edges observed by ARM SWS. *Geophys. Res. Lett.* 36 (16), L16802. <http://dx.doi.org/10.1029/2009gl039366> ISSN 0094-8276.
- Perry, K.D., Hobbs, P.V., 1996. Influences of isolated cumulus clouds on the humidity of their surroundings. *J. Atmos. Sci.* 53 (1), 159–174. [http://dx.doi.org/10.1175/1520-0469\(1996\)053%3C0159:ioicco%3E2.0.co;2](http://dx.doi.org/10.1175/1520-0469(1996)053%3C0159:ioicco%3E2.0.co;2).
- Pilewskie, P., Pommier, J., Bergstrom, R., Gore, W., Howard, S., Rabbette, M., Schmid, B., Hobbs, P.V., Tsay, S.C., 2003. Solar spectral radiative forcing during the Southern African Regional Science Initiative. *J. Geophys. Res.* 108 (D13), 8486. <http://dx.doi.org/10.1029/2002JD002411>.
- Redemann, J., Zhang, Q., Russell, P.B., Livingston, J.M., Remer, L.A., 2009. Case studies of aerosol remote sensing in the vicinity of clouds. *J. Geophys. Res.* 114 (D6), D06209. <http://dx.doi.org/10.1029/2008jd010774>.
- Ricchiazzi, P., Yang, S., Gautier, C., Sowle, D., 1998. SBDART: a research and teaching software tool for plane-parallel radiative transfer in the earth's atmosphere. *Bull. Am. Meteorol. Soc.* 79 (10), 2101–2114. [http://dx.doi.org/10.1175/1520-0477\(1998\)079%3C2101:sarats%3E2.0.co;2](http://dx.doi.org/10.1175/1520-0477(1998)079%3C2101:sarats%3E2.0.co;2).
- Shipley, S.T., Tracy, D.H., Eloranta, E.W., Trauger, J.T., Sroga, J.T., Roesler, F.L., Weinman, J.A., 1983. A high spectral resolution lidar to measure optical scattering properties of atmospheric aerosols, part I: instrumentation and theory. *Appl. Opt.* 23, 3716–3724.
- Su, W., Schuster, G.L., Loeb, N.G., Rogers, R.R., Ferrare, R.A., Hostetler, C.A., Hair, J.W., Obland, M.D., 2008. Aerosol and cloud interaction observed from high spectral resolution lidar data. *J. Geophys. Res.* 113 (D24), D24202. <http://dx.doi.org/10.1029/2008jd010588>.
- Twohy, C.H., Coakley, J.A., Tahnk, W.R., 2009. Effect of changes in relative humidity on aerosol scattering near clouds. *J. Geophys. Res.* 114 (D5), D05205. <http://dx.doi.org/10.1029/2008jd010991>.
- Twomey, S., Bohren, C.F., 1980. Simple approximations for calculations of absorption in clouds. *J. Atmos. Sci.* 37 (9), 2086–2095. [http://dx.doi.org/10.1175/1520-0469\(1980\)037%25253C2086:SAFCA%25253E2.0.CO;2](http://dx.doi.org/10.1175/1520-0469(1980)037%25253C2086:SAFCA%25253E2.0.CO;2).
- Varnai, T., Marshak, A., 2009. MODIS observations of enhanced clear sky reflectance near clouds. *Geophys. Res. Lett.* 36 (6), 6807. <http://dx.doi.org/10.1029/2008gl037089>.
- Varnai, T., Marshak, A., 2011. Global CALIPSO observations of aerosol changes near clouds. *IEEE Geosci. Remote Sens. Lett.* 8 (1), 19–23. <http://dx.doi.org/10.1109/lgrs.2010.2049982> ISSN 1545-598X.
- Wen, G., Marshak, A., Cahalan, R.F., 2006. Impact of 3-D clouds on clear-sky reflectance and aerosol retrieval in a biomass burning region of Brazil. *Geosci. Remote Sens. Lett.* IEEE 3 (1), 169–172. <http://dx.doi.org/10.1109/lgrs.2005.861386> ISSN 1545-598X.
- Yang, W., Marshak, A., Varnai, T., Liu, Z., 2012. Effect of CALIPSO cloud aerosol discrimination (CAD) confidence levels on observations of aerosol properties near clouds. *Atmos. Res.* 116, 134–141.
- Zhang, J., Reid, J.S., Holben, B.N., 2005. An analysis of potential cloud artifacts in MODIS over ocean aerosol optical thickness products. *Geophys. Res. Lett.* 32 (15), L15803. <http://dx.doi.org/10.1029/2005gl023254>.